




Article

Synthesis and Sintering of Tungsten and Titanium Carbide: A Parametric Study

Alma Terlikbaeva ¹, Aliya Alimzhanova ^{1,*} , Zhanna Ereemeeva ², Anar Mukhametzhanova ¹, Galimzhan Maldybaev ¹ , Roza Shayahmetova ¹, Mohammad Abedi ²  and Dmitry Moskovskikh ^{2,3} 

¹ National Center on Complex Processing of Mineral Raw Materials of the Republic of Kazakhstan, Jandossov Str. 67, Almaty 050036, Kazakhstan

² Research Center “Structural Ceramic Nanomaterials”, National University of Science and Technology MISIS, Leninskiy Prospekt 4, 119049 Moscow, Russia

³ Research Laboratory of Scanning Probe Microscopy, Moscow Polytechnic University, 38 B. Semenovskaya St., 107023 Moscow, Russia

* Correspondence: aliyuchca@mail.ru

Abstract: The three primary steps in the production of tungsten carbide WC and titanium carbide TiC powders are the preparation of the green mixture, carbidization by furnace annealing, and ball milling of the annealed products. This work performed a comprehensive parametric investigation of these three steps. The impact of several factors was examined including the carbon precursor, the mass and diameter of the milling bodies (balls), the milling time and speed, the temperature and length of the annealing process, the height of the powder in the furnace boats, and the rate at which the furnace boats move. Regression models for every stage of the process were verified by 10-fold validation and used to optimize the synthesis sequence, resulting in high-quality WC and TiC with a grain size below 2 microns and a content of free carbon below 0.1%. Additionally, solid solution (W,Ti)C was fabricated by mechanochemical synthesis from the elemental mixtures; however, further modification of this technique is necessary because of the observed relatively high concentration of residual free carbon (0.2–0.8%) and contamination by Fe.

Keywords: tungsten carbide; titanium carbide; carbidization; pressureless sintering; parametric study; statistical analysis



Citation: Terlikbaeva, A.; Alimzhanova, A.; Ereemeeva, Z.; Mukhametzhanova, A.; Maldybaev, G.; Shayahmetova, R.; Abedi, M.; Moskovskikh, D. Synthesis and Sintering of Tungsten and Titanium Carbide: A Parametric Study. *Metals* **2022**, *12*, 2144. <https://doi.org/10.3390/met12122144>

Academic Editor: Yadir Torres Hernández

Received: 5 November 2022

Accepted: 6 December 2022

Published: 14 December 2022

Publisher’s Note: MDPI stays neutral with regard to jurisdictional claims in published maps and institutional affiliations.



Copyright: © 2022 by the authors. Licensee MDPI, Basel, Switzerland. This article is an open access article distributed under the terms and conditions of the Creative Commons Attribution (CC BY) license (<https://creativecommons.org/licenses/by/4.0/>).

1. Introduction

Hard alloys based on the refractory carbides of transitory metals contained in one or two metal binders are used in particular to satisfy increased performance requirements for cutting procedures [1]. Carbides are often utilized in cutting tools or coatings due to the carbide’s great hardness and durability, leading to enhanced performance and cost-efficiency of the machining tools [2,3]. The most popular materials for drilling, stamping, and cutting instruments are hard alloys based on tungsten carbide (WC), particularly those doped with Co [4]. Numerous industrial uses for tungsten carbide (WC) and its composites include wear-resistant components for hot rolling mills and drawing dies, mining and cutting tools, precise drilling tips, and sandblast nozzles [5]. Recently, WC has been employed in the catalysis industry to replace noble metals such as palladium (Pd), platinum (Pt), and iridium (Ir) [6]. In proton exchange membrane (PEM) fuel cells, it may also be utilized as a catalyst. Its special qualities including high hardness and strength, superior corrosion resistance, high-temperature stability, and high Young’s modulus are relevant to all of these uses. The main issue with these alloys is their high cost, which is a result of the expenditure involved in producing the original WC and Co powders. The major causes of such are the prohibitively expensive conventional methods of producing WC powder and the slow rates of solid-phase reaction.

There are several ways to make WC powder including heating tungsten–carbon mixtures in carbon tubes to temperatures of 2800 °C in microwave ovens or interacting them with hydrogen, methane, and vacuum at temperatures of 1400–2000 °C [4,7]. Typically, W metal and C are combined in a solid-state process at temperatures between 1200 and 2000 °C in a controlled environment to produce tungsten carbide. This procedure is expensive due to the high temperatures and extended time required by the slow diffusion rates of solid-state reactions. Due to the effective wetting of liquid Co to WC, this ensures the efficient liquid phase sintering of hard metal [8–12]. Co is used extensively as an alloying compound to increase the mechanical strength and corrosion resistance of WC alloys, although doing so raises the cost of manufacture [13–16]. Ni, Cr, Cu, Mo, Al, Si, and Fe are other elements that are accessible and have comparable effects [17–21]. Transient metal carbides such as TiC, TaC, and NbC are frequently used to enhance the properties of WC–Co hard alloys to reduce diffusion wear caused by the γ -phase (Ti, Ta, Nb, W)C that forms during sintering [1,12,22]. TiC carbide is the most desirable material for the doping of WC–Co systems from a scientific and industrial standpoint. The potential for TiC to be used as a doping agent is related to its physical, chemical, mechanical, and operational properties [23]. The primary causes of the high strength, high durability, and heat resistance of WC–TiC–Co alloys include the good thermal stability and great oxidation stability of TiC.

In the hard alloy WC–TiC–Co, there are four distinct phases: WC, TiC, (Ti,W)C, and Co binder. The metallic binder ensures efficient densification during sintering due to the high wettability of the carbide particles by cobalt. Crucially, the cobalt binder also endows the hard alloy with increased fracture toughness (resistance towards dynamic impacts) due to the binder's plasticity. The microstructure and mechanical characteristics of WC–TiC–Co carbides are significantly influenced by the WC/TiC granulometric ratio [24]. The TiC component in WC–TiC–Co alloys typically does not exceed 18 weight percent because TiC is significantly more brittle than WC [25]. Since the ionic radii between W and Ti are similar, WC and TiC form (Ti,W)C solid solution. Typically, the (W,Ti)C grains have a core-shell structure [26]. The rim includes the (Ti,W)C phase with a greater W concentration whereas the core contains the original TiC or (Ti,W)C powder [26]. The partial dissolving of TiC and WC in the liquid-fluid binder and subsequent epitaxial deposition of the solid solution (Ti,W)C on the undissolved TiC grains cause the development of the rim around the TiC grains [27]. Small amounts of TiC additives cause all of the raw TiC grains to dissolve in the binder, leaving just grains (Ti,W)C [28]. Because W atoms do not penetrate TiC well, their distance of diffusion from the rim to the nucleus is only a few nanometers [29]. The microstructure of WC–TiC–Co carbides is dispersed with bigger (Ti,W)C and TiC phases as reinforcement for the WC–Co matrix. WC grains are smaller than TiC grains. The cutting efficiency and performance of hard-alloy bits are improved by doping WC–Co with sub-micron TiC [30–33]. This is carried out to make the bits harder, more wear-resistant, and less susceptible to thermal softening during cutting.

Rigid technological requirements and a slow rate of solid-phase reaction define conventional methods for producing WC, TiC, and Ti (C, N) powders [4,7]. Recently, different methods have been employed to create tungsten carbide particles [34] including the spray conversion process (SCP) [35], chemical vapor deposition (CVD) [36], combustion synthesis (CS) [37–39], wire explosion process, and mechanical alloying (MA) [40,41]. Mechanical alloying is one of the most alluring of these techniques [41]. It is easy to use, does not require expensive machinery or high temperatures, and may also be used to reduce metal oxides and manufacture hard alloys using much cheaper oxide precursors rather than elemental powders [40,42]. The mechanochemical synthesis of transitional metal carbides from chloride precursors has also been reported. [43] The reduction of oxide or chloride precursors is achieved by the addition of a reducing agent—most often magnesium or calcium hydride. The reaction between the reducing agent and oxide is highly exothermic, leading to rapid heating in the contact area between the solid phases, which in turn promotes solid-state diffusion [40,44–48]. High-temperature mechanochemical synthesis (HMS) is a common method for mechanochemical activation, which speeds up the solid-phase interac-

tion of reaction mixture components [45,49,50]. The potential use of mechanically induced solid-phase processes is connected to their usage in technology, particularly in developing novel “dry” technological processes that are more economical and ecologically friendly than the current ones. The mechanochemical synthesis of metal powders involves the use of substances that change the structure and properties of powders under non-equilibrium conditions of particle formation at significant temperature and pressure gradients, which are responsible for starting physical and chemical processes such as phase transitions and chemical reactions [44,45]. However, despite the evident advantages of the mechanochemical synthesis, the phase purity of the product, conversion rate, and possible contamination due to the wear of the milling bodies (steel balls) remains a concern [51]. Therefore, the mechanochemical synthesis of carbide ceramics for hard alloys has to be compared to traditional furnace-based manufacturing to check which technique is more viable.

Mechanochemical synthesis is not the only way to produce desirable carbide ceramics from inexpensive oxide precursors. One of the alternatives was suggested by Koc, who developed a three-step process in which the oxide powders were first coated with carbon by the cracking of propylene (C_3H_6); second, mixed with a substantial amount of carbon black; and finally treated at temperatures in the range of 600–1400 °C for 2 h in flowing Ar or 10% H_2 -Ar atmosphere to synthesize WC. Wang et al. [52] reported that high-quality WC powders of 100 nm size can be synthesized by carbothermal reduction using acetylene black as a carbon source [53]. Ke et al. achieved one-step synthesis and sintering of WC-Co and WC-(Ti,W)C-Co hard metals using carbon black, Co, WO_3 , and TiO_2 as raw materials by combining the carbothermal reduction of oxides and the liquid phase sintering of hard metal in one annealing cycle [54,55]. The heating rate plays an important role in controlling the carbide particle growth mechanism [56]. Sub-10 nm carbide particles can be produced by carefully controlling the sintering conditions, which accentuates the necessity for the development of comprehensive predictive models of the milling and annealing operations in the carbide production cycle [57].

Currently, there is a lack of systematic multi-parameter statistical investigations of WC and TiC synthesis, since most published articles performed a limited single-parameter optimization. In particular, no comparisons are available between the intermittent and continuous sintering modes in furnaces as well as between conventional furnace synthesis and mechanochemical synthesis. In this work, a systematic parametric study was performed on the synthesis of WC, TiC, and WC-TiC powders by the means of high-temperature synthesis and mechanochemical synthesis. The sintering experiments were performed using three carbon precursors, a range of milling conditions employed for the preparation of the reactive mixture and for refinement of sintering products (diameter of milling bodies 16–32 mm, ball mass 200–300 g, milling time 30–150 min, milling speed 20–40 rpm), and sintering conditions (temperature interval of 1000–1700 °C, duration 30–150 min, the height of powder in the boats was 10–20 mm, boat movement speed 10–25 mm/min) were investigated. For the mechanochemical synthesis, the duration of 15–60 min was used. Detailed regression models were constructed for the investigated processes to enable improved control of the synthesis.

2. Materials and Methods

The following powders were used as precursors: (I) Metals Ti and W (RusRedMet, St Petersburg, Russia) with a purity of >99% and a particle size within the range of 40–60 μm and (II) three forms of carbon powders: carbon black, GISM grade graphite, GK grade graphite, with a purity of 99% and a particle size of 7–10 μm . Mixtures of the following compositions were used: WC—93.9% W + 6.1% C; TiC—80% Ti + 20% C; (W,Ti)C—71.9% W + 18.8% Ti + 9.3% C.

Elemental powder mixtures were prepared using the ball mill WiseMixSBML (DAIHAN Scientific, Wonju-Si, Republic of Korea) equipped with 250 mL steel jars and 6 mm steel balls. The different sintering runs constituting the experimental matrix were conducted in a graphite tube furnace in a nitrogen atmosphere. For each run, at least three

samples were sintered concurrently. Two sintering modes were employed. In the first (intermittent) mode, the alumina boat with the samples was placed in the middle of the furnace's hot zone, then the furnace was heated to the sintering temperature at a rate of 10 °C/min, followed by a soak at the dwelling temperature for a specific time, and free cooling to the room temperature. In the second (continuous) mode, the furnace was heated up to the sintering temperature, then the boat containing the sample was inserted at the beginning of the furnace and moved through the furnace at a certain speed, referred to as the boat movement speed. The experiments in the second mode were conducted to emulate the conditions relevant to continuously operating industrial furnace equipment.

For the mechanochemical synthesis of (W,Ti)C, 18 g batches of W + Ti + C mixture were used for HEBM treatment in a double-station planetary ball mill (Activator-2s, Activator, Moscow, Russia). The ball (stainless steel, 6 mm in diameter) to powder mixture weight ratio was 20:1. Before milling, the jar (stainless steel, 250 mL incapacity) was sealed, vacuumed, and filled with 99.998% pure argon up to 4 atm. The milling speed was 694 rpm at a rotational coefficient of $K = 1$.

The size of the resulting powders was determined via laser diffraction analysis using a Fritsch Analysette 22 Microtec Plus instrument (Fritsch, Idar-Oberstein, Germany). As-milled composite ceramic powders were subjected to magnetic separation using an LSV dry separator (SOLLAU, Velký Ořechov, Czech Republic) for the elimination of iron impurities. The phase composition of the synthesized and sintered powders was measured by XRD analysis on a Dron-4 installation (JSC "Burevestnik", Saint-Petersburg, Russia) using $\text{CuK}\alpha$ radiation, 2θ range 10–110°, 0.1° step, and 6 s exposition time. Spectra were treated using the JCPDS database (International Centre for Diffraction Data, Newtown Square, PA, USA).

Free carbon content (C_{free}) was measured using a modified Meerson–Samsonov technique (i.e., wet chemical dissolution in hot chromic–sulfuric–iodic acid mixtures. All free carbon during the dissolution was oxidized to carbon dioxide, which was measured coulometrically as a function of the oxidation time [58]. Total carbon content (C_{total}) was measured using the elemental analyzer ELEMENTRAC CS-i (Eltra GmbH, Haan, Germany) using combustion in an induction furnace and the subsequent analysis of the gaseous carbon dioxide.

The structures of powdered and compact materials were studied by scanning electron microscopy (SEM) on an S-3400 N microscope (Hitachi, Tokyo, Japan) equipped with a NORAN energy-dispersive X-ray spectrometer (EDX) (Thermo Fisher Scientific, Waltham, MA, USA). The average grain size was measured from SEM micrographs of a milled powder, using a line-intercept method and taking into account at least 50 grains. A three-dimensional correction factor of 1.2 was used, meaning that individual grains were approximated by spheres. For the measurements, a confidence interval (95%) was used, which corresponded to 2 sigma on each side of the mean.

The mixture quality coefficient Q was calculated based on the variance in the particle distribution observed by SEM and EDS. After the imaging of the samples, random secants were drawn, and the component particles were recorded in the order in which the secant line intersects them. After the data collection, analysis of variance (ANOVA) was performed on the dataset to ascertain the homogeneity of the mixture (higher variance corresponds to better mixing). The variance contains three parameters: mixture variance, analytical variance, and sampling variance. The variability due to sampling is very difficult to determine, thus, in practice, it is usually neglected. The analytical variance was determined by the repetition of the measurements on the same samples. It is important to note that the parameter Q does not represent the true variance in the mixture composition, but rather a convolution between it and other variance sources. This estimation was taken into account by calculating a confidence interval (95%) that corresponded to 2 sigma on each side of the mean.

The statistical treatment of the data produced in the parametric study was treated using Minitab 21.1 software (Pennsylvania State University, Pennsylvania, PA, USA). Regression models were constructed for every dataset and further used for response optimization.

Individual desirability was calculated for each response and weighted by the importance assigned to it on a scale from 1 to 10. It should be noted that the importance score has to be selected arbitrarily by the investigator. These values were combined to determine the composite, or overall, the desirability of the multi-response system. An optimal solution occurs where composite desirability obtains its maximum. Therefore, the response optimization is most effective when interpreted in conjunction with relevant subject matter expertise including background information, theoretical principles, and knowledge obtained through observation or previous experimentation.

3. Results and Discussion

In this work, five datasets were produced in relation to the furnace synthesis of TiC and WC and used to construct regression models (Supplementary Tables S1–S12, Supplementary Figures S1–S6).

3.1. Titanium Carbide Synthesis

Regression analysis was performed with the C_{free} , C_{total} , and TiC grain size outputs vs. temperature (T) and carbon source inputs using 10-fold cross-validation and the stepwise selection of terms (α to enter = 0.15, α to remove = 0.15). The initial dataset is provided in Supplementary Table S1. The Pareto plot of parameter significance and residual plots (normal probability plot, vs. fits, histogram, versus order) are shown in Supplementary Figures S1–S3. The main effects and interaction plots from the derived regression models are presented in Figure 1. Residuals were homoscedastic and normally distributed. For the C_{free} output, the following regression equations (Equations (1)–(3)) were obtained for the three used carbon precursors (Figure 1c):

$$\text{For Carbon black precursor: } C_{free, \%} = -1.31 + 0.00349 T - 0.000001 \times T^2 \quad (1)$$

$$\text{For GISM precursor: } C_{free, \%} = 10.25 - 0.01161 T + 0.000004 \times T^2 \quad (2)$$

$$\text{For GK precursor: } C_{free, \%} = 1.80 - 0.00060 \times T \quad (3)$$

where T—temperature, °C.

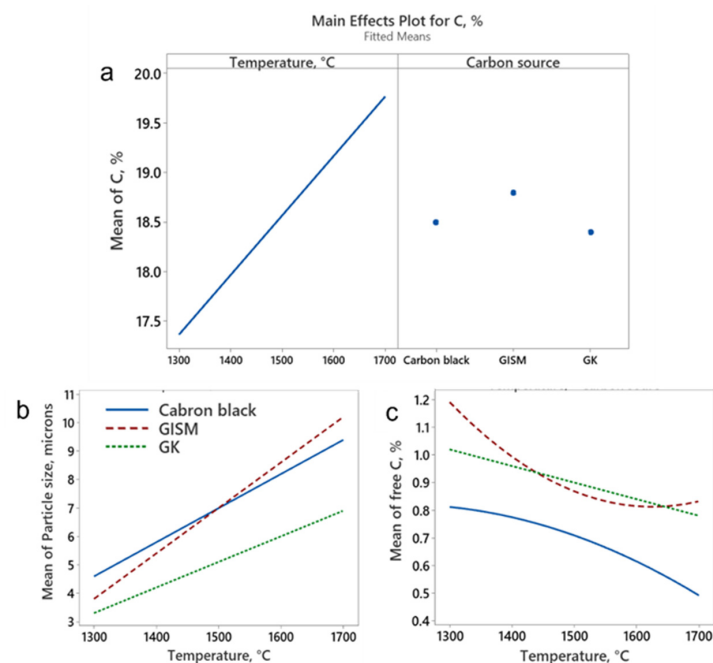


Figure 1. Main effect plots for the influence of temperature and carbon precursor on the total carbon content (a), free carbon content (b), and average TiC particle size (c).

For the GK precursor, the free carbon content showed a linear dependence on temperature (T). For the precursors carbon black and GISM, the dependences had a weak quadratic term. A cutoff threshold of 1.65 was used to select statistically significant members of the model. The adjusted R^2 (coefficient of determination) for the model was 89.74%; however, the 10-cross validation produced a relatively low R^2 value of 40.02% (Supplementary Table S2). This might be related to the partial overfitting of the model in relation to the influence of GISM precursor on the free carbon content, since the fitted curve showed a counter-intuitive inflection point at ~ 1550 °C (Figure 1c).

Supplementary Table S3 provides the detailed characterization of the constructed regression model of grain size evolution during TiC carbidization. The adjusted R^2 for the model was 94.75%; the 10-cross validation produced an R^2 value of 87.89% (Supplementary Table S3). Supplementary Figure S2 provides the Pareto chart of the standardized coefficients and residual plots for the constructed regression model of TiC grain size evolution during TiC carbidization. A cutoff threshold of 1.574 was used to select statistically significant members of the model. Residual distribution was homoscedastic and normally distributed.

For the particle sizes, the following regression equations (Equations (4)–(6)) were obtained (Figure 1b):

$$\text{Carbon black: Particle size (microns)} = -11.00 + 0.01200 \times T \quad (4)$$

$$\text{GISM: Particle size (microns)} = -17.00 + 0.01600 \times T \quad (5)$$

$$\text{GK: Particle size (microns)} = -8.40 + 0.00900 \times T \quad (6)$$

where T—temperature, °C.

For the total carbon content (Figure 1a), the following regression equations were obtained (Equations (7)–(9)):

$$\text{Carbon black: } C_{\text{total}} (\%) = 9.500 + 0.006 \times T \quad (7)$$

$$\text{GISM: } C_{\text{total}} (\%) = 9.800 + 0.006 \times T \quad (8)$$

$$\text{GK: } C_{\text{total}} (\%) = 9.400 + 0.006 \times T \quad (9)$$

where T—temperature, °C.

Supplementary Table S4 provides the detailed characterization of the constructed regression model of grain size evolution during TiC carbidization. The adjusted R^2 for the model was 89.61%; the 10-cross validation produced an R^2 value of 89.55% (Supplementary Table S4). Supplementary Figure S3 provides the Pareto chart of the standardized coefficients and residual plots for the constructed regression model of the total carbon content in TiC after carbidization. A cutoff threshold of 1.55 was used to select statistically significant members of the model. Residual distribution was homoscedastic and normally distributed.

Overall, the increase in temperature increased the total carbon content, and decreased the content of free carbon (although in the case of the GISM carbon precursor, the model predicted a slight increase in free carbon content above 1550 °C, probably indicating overfitting of the model), and produced larger TiC grains (Figure 1).

The developed model was used for response optimization. From the three output parameters (total carbon content, free carbon content, TiC grains size), the optimal outcome was the maximum total carbon content, minimum free carbon content, and minimum TiC grain sizes. Since the maximum carbon content and minimum TiC grain sizes are mutually contradictory (an increase in temperature leads to lower free C content, but results in grain coarsening—Figure 1b,c), they were assigned different importance: 10 for total C content and free C content, and 2 for TiC grain size. The weight of all targets was chosen as 1 (Table 1). Three solutions were generated (Table 1) and compared using a composite desirability metric. The best composite desirability was achieved for solution 1—annealing at 1700 °C using carbon black precursor, which was predicted to produce

TiC with a 9.4 micron size, 0.49% free C, and 19.7% total C content. Confidence intervals, prediction intervals, and standard error fits are also provided in Table 1.

Table 1. Response optimization for the TiC carbidization process based on the developed regression model. SE—standard error, CI—confidence interval, PI—prediction interval.

| Parameters | | | | | | | |
|------------------------|-----------------|------------------------|----------------------------|---------------|------------------|------------------------|--------------|
| Response | Goal | Lower | Target | Upper | Weight | Importance | |
| Particle size, microns | Minimum | | 3.5 | 11.0 | 1 | 2 | |
| free C, % | Minimum | | 0.5 | 1.2 | 1 | 10 | |
| C, % | Maximum | 17 | 20.0 | | 1 | 10 | |
| Solutions | | | | | | | |
| Solution | Temperature, °C | Carbon Source | Particle Size, microns Fit | free C, % Fit | C, % Fit | Composite Desirability | |
| 1 | 1700.00 | Carbon black | 9.4 | 0.49 | 19.7 | 0.82 | |
| 2 | 1700.00 | GK | 6.9 | 0.78 | 19.6 | 0.70 | |
| 3 | 1644.81 | GISM | 9.3 | 0.81 | 19.7 | 0.63 | |
| Prediction Confidence | | | | | | | |
| Variable | Setting | Response | Fit | SE Fit | 95% CI | 95% PI | Measurements |
| Temperature, °C | 1700 | Particle size, microns | 9.4 | 0.374 | (8.554, 10.246) | (8.018, 10.782) | 8.9 ± 1.3 |
| Carbon source | Carbon black | free C, % | 0.49 | 0.052 | (0.3643, 0.6186) | (0.3059, 0.6769) | 0.51 ± 0.17 |
| Variable | Setting | C, % | 19.7 | 0.146 | (19.379, 20.021) | (19.059, 20.341) | 19.3 ± 1.1 |

CI—confidence interval, PI—prediction interval, SE—standard error of the regression.

3.2. Homogenization of W + C Mixture before Furnace Annealing

Regression analysis was performed with mixture homogeneity Q (%) output vs. ball diameter, mm (D), ball mass, g (M), milling time, min (t), and mill rotations per minute (V) input using 10-fold cross-validation and the stepwise selection of terms (α to enter = 0.15, α to remove = 0.15). The initial dataset is provided in Supplementary Table S5. The Pareto plot of parameter significance and residual plots (normal probability plot, vs. fits, histogram, vs. order) are shown in Supplementary Figure S4. A cutoff threshold of 1.50 was used to select statistically significant members of the model. Residual distribution was homoscedastic and normally distributed. The model showed very high coefficients of determination. The adjusted R^2 for the model was 98.50%; the 10-cross validation produced an R^2 value of 96.77% (Supplementary Table S6). The following regression equation was obtained (Equation (10)):

$$Q = -89.5 + 1.746 \times D_b + 1.186 \times M_b + 0.0553 \times t_m + 0.0256 \times V - 0.02667 \times D_b^2 - 0.002350 \times M_b^2 - 0.00037 \times t_m^2 + 0.002216 \times t_m \times V_m \quad (10)$$

where Q is the coefficient of homogeneity; D_b is ball diameter (mm); M_b is ball mass (g); t_m is milling time (min); and V_m is the milling speed (rotations per minute).

The main effects plot for the mixture homogeneity is shown in Figure 2. The mixture homogeneity increased linearly with the increase in the ball diameter. The ball mass had a nonlinear effect on the mixture homogeneity—an increase in ball mass from 200 to 250 g improved the mixture homogeneity, whereas a further increase in the ball mass to 300 g decreased the mixture homogeneity. The increased milling time resulted in a nearly linear improvement in the mixture homogeneity. The rotational speed had a less pronounced nearly linear effect.

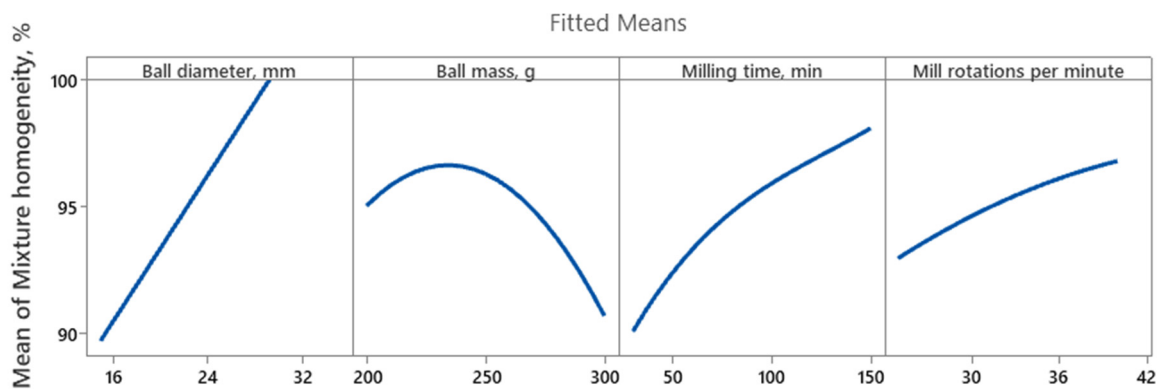


Figure 2. Main effects plot for mixture homogeneity.

The two-parameter interaction plots were constructed based on the developed regression model to analyze the interplay between the investigated parameters (Figure 3). For every plot, two of the parameters were fixed and two were varied along the X and Y axes. When ball mass and milling time were fixed, the homogeneity increased nearly linearly with an increase in the milling speed and ball diameter (Figure 3a), and a homogeneity of 92–95% was achieved at a 35-mm ball diameter and 40 rotations per minute (rpm) milling speed. When the ball diameter and milling speed were fixed (Figure 3b), the dependence of mixture homogeneity on the ball mass and milling time reached a maximum (>95%) at the intermediate ball mass value (260 g) and the highest tested milling time (150 min). When the milling time and milling speed were fixed (Figure 3c), the highest mixture homogeneity (>98%) was achieved at the smallest investigated ball mass (200 g) and largest investigated ball diameter (35 mm). When the ball diameter and ball mass were fixed (Figure 3d), the highest mixture homogeneity (>98%) was achieved at the highest investigated milling speed and duration. With the ball mass and milling speed fixed (Figure 3e), the highest homogeneity (>95%) was achieved at an intermediate milling time (~120 min) and the highest ball diameter (35 mm). With the ball diameter and milling time fixed, the highest homogeneity was achieved at the intermediate ball mass (230–250 g) and highest milling speed (37.5–40 rpm).

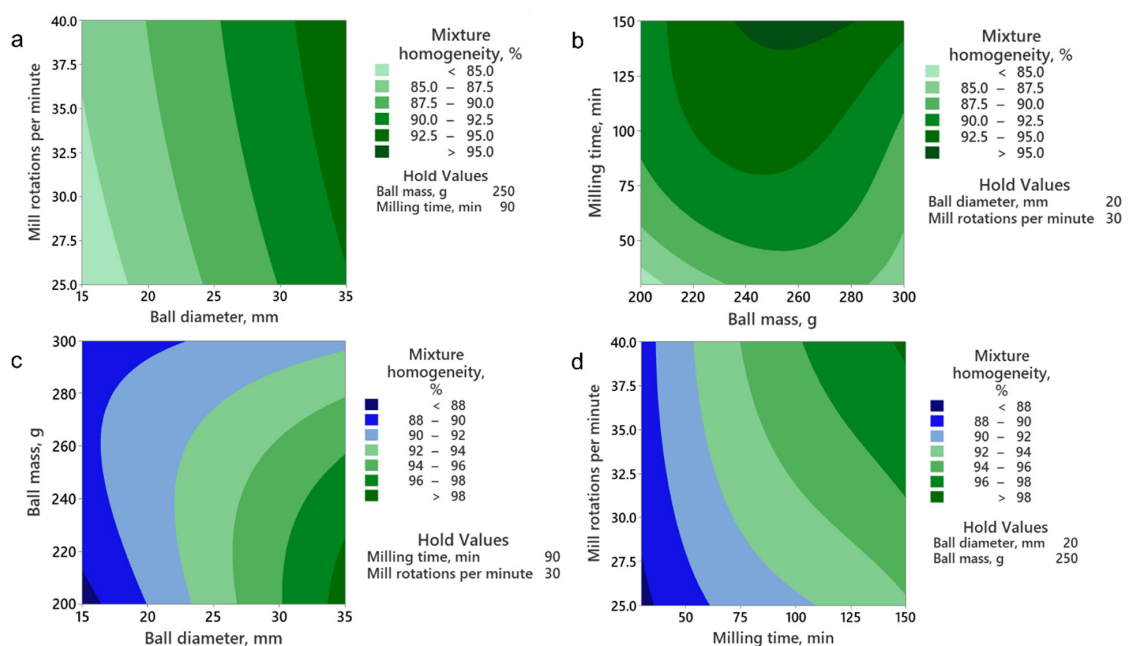


Figure 3. Cont.

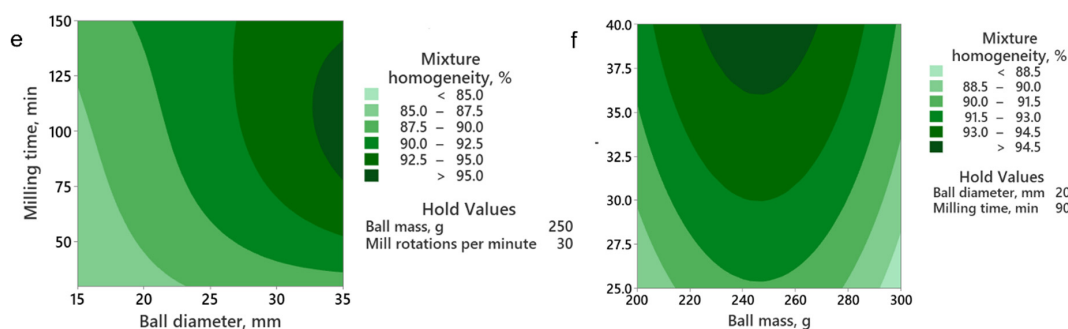


Figure 3. Interaction plots for the W + C mixture homogeneity after ball milling. Interaction plots represent the combined influence of mill rotations per minute and ball diameter (a), milling time and ball mass (b), ball mass and ball diameter (c), milling speed and milling duration (d), milling duration and ball diameter (e), and milling speed and ball mass (f).

Since both main effects (Figure 2) and two-parameter interactions (Figure 3) had some strong nonlinearity, the regression model is particularly useful for finding the globally optimal solution (100% mixture homogeneity). Two solutions were generated (Table 2) and compared using a composite desirability metric. A desirability of 1 was achieved for both solutions, indicating that a 100% mixture homogeneity could be attained using two different mixing conditions: (1) 25 mm balls, 250 g ball mass, 117 min milling time, 40 rotations per minute, and (2) 35 mm balls, 217 g ball mass, 150 min milling time, and 40 rotations per minute. The confidence intervals, prediction intervals, and standard error fits are also provided in Table 2. The first developed mixing condition combination (25 mm balls, 250 g ball mass, 117 min milling time, 40 rotations per minute) was used to prepare the mixtures for the subsequent carburization.

Table 2. Response optimization for the W + C mixture homogenization based on the developed regression model. SE—standard error, CI—confidence interval, PI—prediction interval.

| Response | Goal | Parameters | | | Weight | Importance | |
|---------------------------|-------------------|------------------------|-------------------|---------------------------|----------------------------|------------------------|--------------|
| | | Lower | Target | Upper | | | |
| Mixture homogeneity, % | Target | 78 | 100 | 110 | 1 | 1 | |
| Solutions | | | | | | | |
| Solution | Ball diameter, mm | Ball mass, g | Milling time, min | Mill rotations per minute | Mixture homogeneity, % Fit | Composite Desirability | |
| 1 | 25 | 250 | 117 | 40 | 100 | 1.00 | |
| 2 | 35 | 217 | 150 | 40 | 100 | 1.00 | |
| Prediction confidence | | | | | | | |
| Variable | Setting | Response | Fit | SE Fit | 95% CI | 95% PI | Measurements |
| Ball diameter, mm | 25 | Mixture homogeneity, % | 100 | 0.629 | (98.684, 101.316) | (98.073, 101.927) | 99.1 ± 0.6 |
| Ball mass, g | 250 | | | | | | |
| Milling time, min | 117 | | | | | | |
| Mill rotations per minute | 40 | | | | | | |

CI—confidence interval, PI—prediction interval, SE—standard error of the regression.

3.3. Carburization of Homogenized W + C Mixture in the Furnace

Regression analysis was performed with the free carbon content (%) output versus temperature, °C (T), annealing duration, min (t_a), the height of powder in the boats, mm (h_p), and boat movement speed, mm/min (V_a) input parameters, using 10-fold cross-

validation and the stepwise selection of terms (α to enter = 0.15, α to remove = 0.15). The initial dataset is provided in Supplementary Table S7. Pareto plots of parameter significance and residual plots (normal probability plot, vs. fits, histogram, vs. order) are shown in Supplementary Figures S4 and S5. A cutoff threshold of 1.485 was used to select statistically significant members of the model. Residual distribution was homoscedastic and normally distributed. The adjusted R^2 for the model was 92.97%; the 10-cross validation produced an R^2 value of 91.86% (Supplementary Table S8). Since the dataset related to the continuous annealing mode was collected separately, the dataset and model parameters are provided in Supplementary Tables S9 and S10.

The following regression equations were obtained (Equations (11) and (12)):

$$\text{Free carbon, \%} = 8.26 - 0.00996 \times T - 0.001542 \times t_a + 0.02433 \times h_p + 0.000003 \times T^2 \quad (11)$$

$$\text{Free carbon, \%} = 55.64 - 0.08056 \times T + 0.1265 \times V_a + 0.000029 \times T^2 - 0.000084 \times T \times V_a \quad (12)$$

where T —temperature, °C; t_a —annealing duration, min; h_p —the height of powder in the boats, mm; V_a —boat movement speed, mm/min.

The main effects plot for the free carbon content in WC after annealing is shown in Figure 4. The free carbon content decreased nonlinearly with an increase in temperature. The minor inflection point on the free carbon vs. annealing temperature curve at ~1050 °C was an artifact of the quadratic equation and should be disregarded. The increase in annealing duration linearly decreased the content of free carbon. Interestingly, the free carbon content increased linearly with the increase in the height of powder in the boats. This increase is probably related to the uneven distribution of the temperature field in the furnace. The boat movement speed did not affect the free carbon content in the 10–20 mm/min interval, but the increase in boat movement to 25 mm/min caused a rise in the free carbon content due to insufficient soaking of the annealed mixture in the high-temperature zone of the furnace.

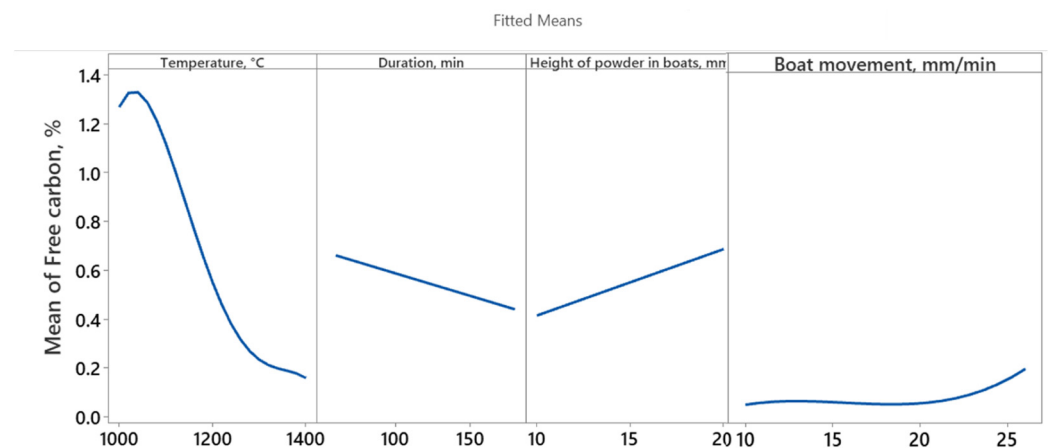


Figure 4. Main effect plots for the free carbon content in WC after the carbidization in the furnace.

The two-parameter interaction plots were constructed based on the developed regression model (Figure 5). At $T \geq 1400$ °C, the free carbon content was below 0.2% at all investigated annealing durations (Figure 5a). Similarly, at $T \geq 1300$ °C, the content of free carbon was below 0.3% at all investigated boat movement speeds (Figure 5b). This is unsurprising since the boat movement is analogous to the annealing duration. Interestingly, the increase in the height of the powder in the boat always led to an increase in the free carbon content. At 120 min annealing duration, the free carbon content below 0.2% could be achieved only at the height of the powder in the boats below 16 mm and temperatures above 1300 °C (Figure 5c). For the fixed temperature, the duration of annealing and the height of powder in the boats required to achieve a certain free carbon content had a linear relationship (Figure 5d). A free carbon content below 0.3% could be achieved at a height of

powder below 13 mm and an annealing duration above 130 min. Details for the regression analysis are provided in Table S10.

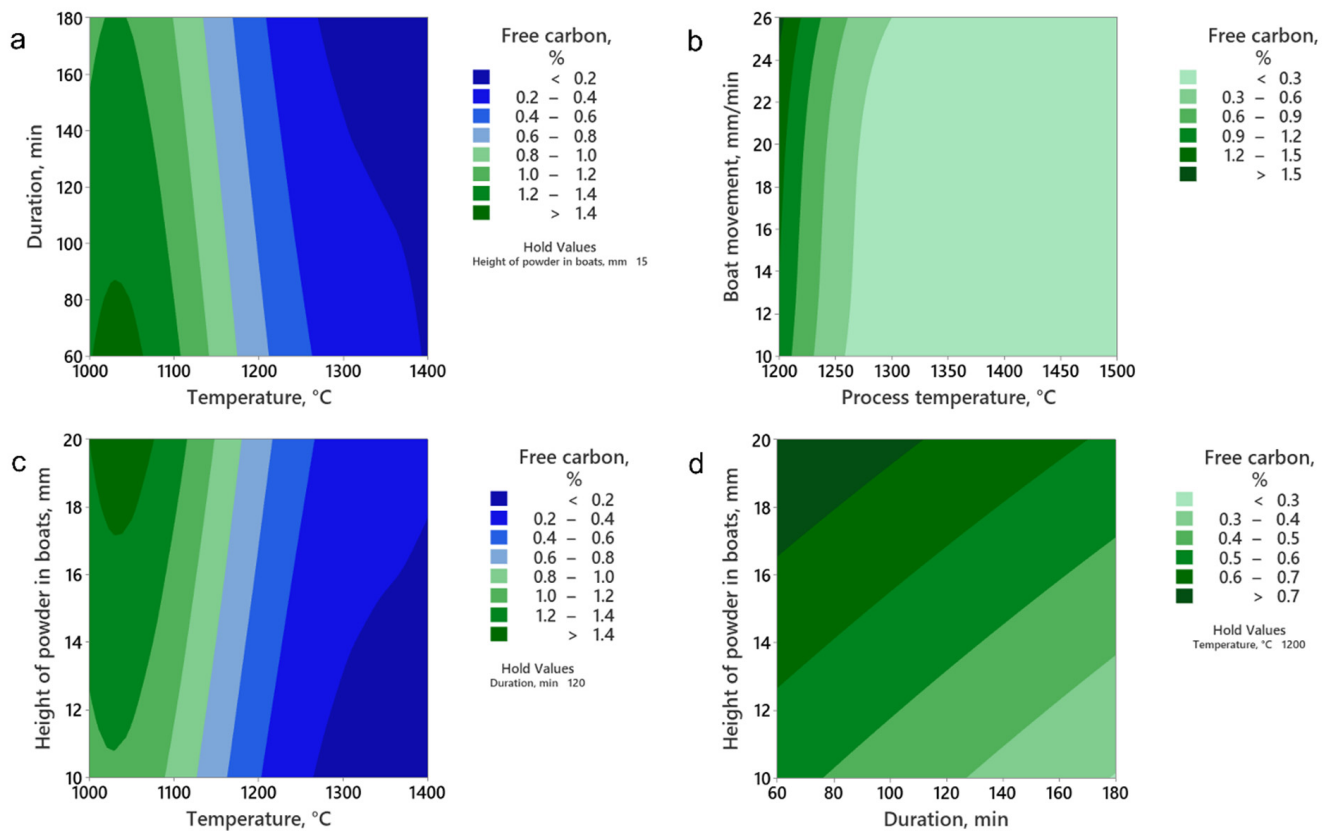


Figure 5. Two-parameter interaction plots for the free carbon content in WC after annealing in a furnace. Interaction plots represent the combined influence of duration and temperature (a), boat movement and process temperature (b), the height of powder in boats and temperature (c), the height of powder in boats, and duration (d).

The developed regression model was used to find the global optimum solutions that would allow for minimizing the content of free carbon in the carbidized WC. Since the annealing duration and boat movement speed essentially represent the same parameter, Equation (11) was used for the optimization. Three solutions were generated (Table 3) and compared using a composite desirability metric. The desirability of 1 was achieved for all three solutions, indicating that a free carbon content below 0.1% could be attained using three different annealing conditions: (1) temperature 1400 °C, duration 107 min, the height of powder in the boats 10 mm; (2) temperature 1400 °C, duration 180 min, the height of powder in the boats 14.65 mm; (3) temperature 1346.5 °C, duration 180 min, the height of powder in the boats 10 mm. Confidence intervals, prediction intervals, and standard error fits are also provided in Table 3. The first developed mixing condition combination (temperature 1400 °C, duration 107 min, height of powder in the boats 10 mm) was used for further experiments on ball milling of the carbidized WC.

Table 3. Response optimization for WC carbidization based on the developed regression model. SE—standard error, CI—confidence interval, PI—prediction interval.

| Parameters | | | | | | | |
|-------------------------------|-----------------|----------------|-------------------------------|--------------------|------------------------|-------------------|--------------|
| Response | Goal | Lower | Target | Upper | Weight | Importance | |
| Free carbon, % | Target | 0 | 0.001 | 1.6 | 1 | 1 | |
| Solutions | | | | | | | |
| Solution | Temperature, °C | Duration, min | Height of powder in boats, mm | Free carbon, % Fit | Composite Desirability | Solution | |
| 1 | 1400.00 | 107 | 10 | 0.001 | 1.00 | 1 | |
| 2 | 1400.00 | 180 | 14.65 | 0.001 | 1.00 | 2 | |
| 3 | 1346.5 | 180 | 10 | 0.001 | 1.00 | 3 | |
| Prediction confidence | | | | | | | |
| Variable | Setting | Response | Fit | SE Fit | 95% CI | 95% PI | Measurements |
| Temperature, °C | 1400 | Free carbon, % | 0.001 | 0.0552 | (-0.1128, 0.1148) | (-0.2880, 0.2900) | 0.15 ± 0.08 |
| Duration, min | 107 | | | | | | |
| Height of powder in boats, mm | 10 | | | | | | |

CI—confidence interval, PI—prediction interval, SE—standard error of the regression.

3.4. Ball Milling of Carbided WC

Regression analysis was performed with the WC grain size (microns) output versus the ball-to-powder ratio, milling duration (min), and milling speed (rotations per minute—rpm) using 10-fold cross-validation and stepwise selection of terms (α to enter = 0.15, α to remove = 0.15). The initial dataset is provided in Supplementary Table S11. Pareto plots of parameter significance and residual plots (normal probability plot vs. fits, histogram vs. order) are shown in Supplementary Figure S6. A cutoff threshold of 1.485 was used to select statistically significant members of the model. Residual distribution was homoscedastic and normally distributed. The following regression equation was obtained (Equation (13)):

$$D_{WC} = 74.64 - 14.82 \times R - 0.0831 \times t_m - 2.133 \times V_m + 2.36 \times R^2 + 0.000196 \times t_m^2 + 0.02548 \times V_m^2 \quad (13)$$

where D_{WC} —WC grains size (microns), R —balls to WC ratio, t_m —milling duration (min), V_m —milling speed (rpm).

The adjusted R^2 for the model was 97.47%; the 10-cross validation produced an R^2 value of 96.87% (Supplementary Table S12). The main effects plot for the WC grain size after ball milling is shown in Figure 6. The two-parameter interaction plots are provided in Figure 7. The WC grain size decreased nonlinearly with the increase in the ball-to-powder ratio, milling duration, and milling speed.

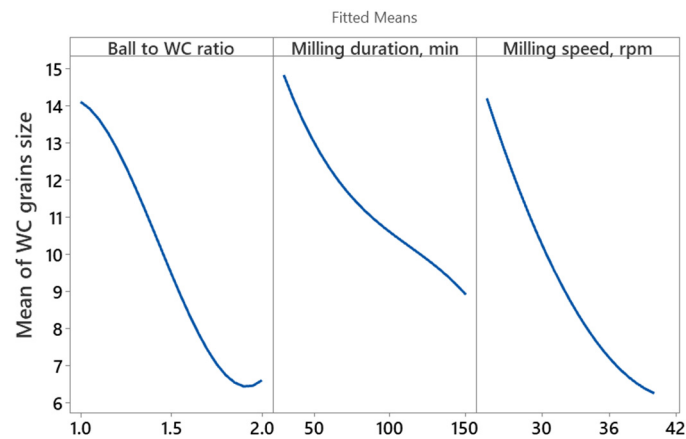


Figure 6. Main effect plots for the grain sizes of carbidized WC after ball milling.

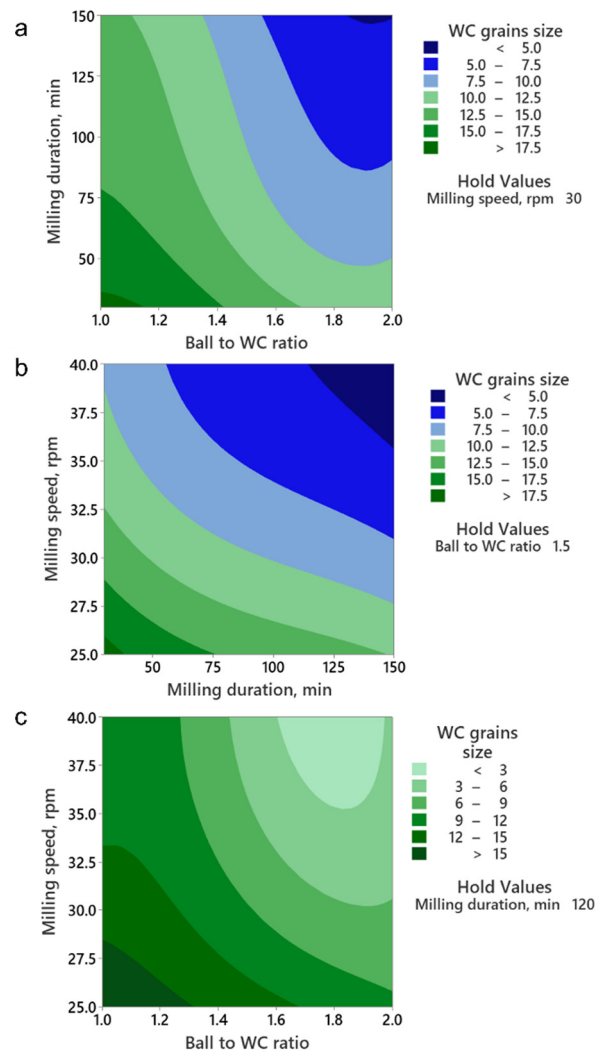


Figure 7. Two-parameter interaction plots for the WC grain sizes after ball milling. Interaction plots represent the combined influence of milling duration and ball-to-WC ratio (a), milling speed and milling duration (b), and milling speed and ball-to-WC ratio (c).

The developed regression model was used to find the global optimum solutions that would allow for minimizing the grain size of the carbidized WC after ball milling. Three solutions were generated (Table 4) and compared using a composite desirability metric.

The desirability of 1 was achieved for two out of three solutions, indicating that a grain size of 1.8 microns could be attained using the following conditions: Ball to WC ratio of 2, milling duration 150 min, milling speed 40 rpm. Confidence intervals, prediction intervals, and standard error fits are also provided in Table 4.

Table 4. Response optimization for WC ball milling after carbidization. SE—standard error, CI—confidence interval, PI—prediction interval.

| Parameters | | | | | | | |
|-----------------------|------------------|-----------------------|--------------------|--------------------|------------------------|-----------------|--------------|
| Response | Goal | Lower | Target | Upper | Weight | Importance | |
| WC grain size | Minimum | | 3 | 22 | 1 | 1 | |
| Solutions | | | | | | | |
| Solution | Ball to WC ratio | Milling duration, min | Milling speed, rpm | WC grains size Fit | Composite Desirability | Solution | |
| 1 | 2 | 150 | 40 | 1.83 | 1.00 | 1 | |
| 2 | 1.8 | 150 | 40 | 3 | 1.00 | 2 | |
| 3 | 1.75 | 150 | 40 | 3.35 | 0.98 | 3 | |
| Prediction confidence | | | | | | | |
| Variable | Setting | Response | Fit | SE Fit | 95% CI | 95% PI | Measurements |
| Ball to WC ratio | 2 | | | | | | |
| Milling duration, min | 150 | WC grains size | 1.83 | 0.421 | (0.967, 2.702) | (−0.104, 3.774) | 1.9 ± 0.4 |
| Milling speed, rpm | 40 | | | | | | |

CI—confidence interval, PI—prediction interval, SE—standard error of the regression.

Figure 8 provides the SEM micrographs of WC after carbidization (1400 °C, 107 min, the height of powder in boats 10 mm; Figure 8a,b) and after subsequent ball milling (ball to WC ratio = 2, milling duration 150 min, milling speed 40 rpm; Figure 8b,c) according to the optimized conditions. The average grain size of the produced WC was below 2 microns, corresponding to the prediction of the model (Figure 8d). The free carbon content in the milled WC was below 0.1%.

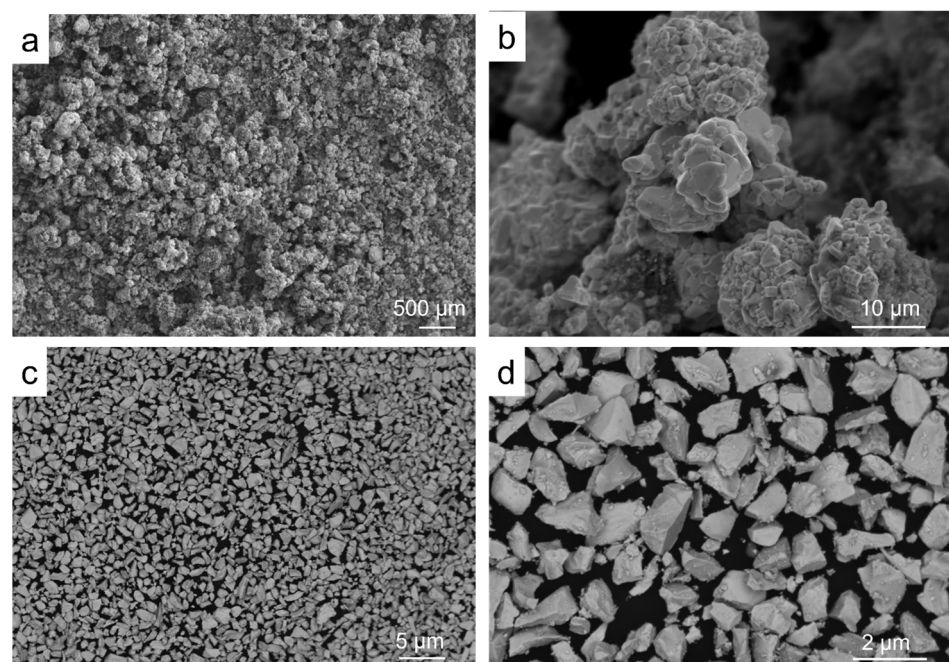


Figure 8. WC after carbidization (a,b) and after ball milling (c,d).

3.5. Mechanochemical Synthesis of WC from an Elemental Mixture

Additionally, the mechanochemical synthesis of complex (W,Ti)C carbide in the high-energy planetary centrifugal mill Activator 4 M was studied. A total of 86.3 g of tungsten powder, 8.4 g of titanium powder, and 3.2 g of carbon black were used to start the carbidization process. Since some carbon black collects on the walls of the drum during the mechanochemical production process, more soot was used. In an argon environment at $p = 3$ to 5 atm, over the course of 5 to 60 min, mechanochemical synthesis was performed using an Activator 4 M planetary ball mill with a planetary disk rotation speed of 800 rpm and drum rotation speed of 1200 rpm. When tungsten powder and carbon black were subjected to mechanochemical treatment for 5–15 min, the existence of unreacted carbon black and tungsten with lattice parameters ($a = 3.155 \text{ \AA}$) was discovered, according to the XRD data. A quantitative study of a mechanically activated equimolar combination of tungsten powder and carbon black revealed some “losses” of the latter, which may have been brought on by soot buildup on the walls of the planetary ball mill.

The complete transformation of the initial powders of tungsten and carbon black occurred when the mixtures were processed for 30 min. When processing for more than 30 min, rubbing of iron on the resulting powder was observed. Table 5 shows the chemical and phase composition of the tungsten carbide powder obtained by the mechanochemical synthesis method.

Table 5. Chemical and phase composition of the mechanochemically synthesized WC.

| Mechanochemical Synthesis Duration, min | Content, w.% | | | Phase Composition | |
|--|--------------|--------|-----|-------------------|------------------|
| | C Total | C Free | Fe | (W,Ti)C | W ₂ C |
| 15 | 4.76 | 0.9 | - | 66.2 | 33.4 |
| 30 | 5.55 | 0.17 | - | 77.8 | 21.9 |
| 45 | 5.6 | 0.16 | 1.1 | 77.5 | 22.1 |
| 60 | 5.61 | 0.14 | 3.6 | 78.2 | 21.3 |

The results in Table 5 and Figure 9 demonstrate that the produced complex carbide did not match the specifications because it contained a sizable quantity of free carbon and iron. It has been demonstrated that (W,Ti)C powder can be produced using mechanochemical synthesis, however, further research needs to be conducted to determine the best mechanochemical synthesis conditions for producing tungsten carbide with a low content of iron and free carbon.

To ascertain the mechanism of formation of the (W,Ti)C solid solution during the mechanochemical synthesis, interface reaction diagrams (Figure 10a,b) were constructed based on the ab initio data from the Materials Project database. Since we did not have a reliable estimation of the temperature within the milling jars during the mechanochemical synthesis, the formation energy values were approximated at 100 °C using the approach developed by Bartel et al. [59]. At this temperature, the W–Ti–C diagram contains four stable binary phases (WTi, WC, TiC, Ti₂C, Ti₈C₅) and one ternary phase Ti₄WC₅, along with five more metastable phases: W₉C₄, W₂C, Ti₃C₂, TiWC₂, Ti₄WC₅. Among these phases, TiC had the highest formation energy (−0.794 eV/atom), while WTi had the lowest (−0.04 eV/atom). Due to its low formation energy, it is unlikely that the WTi intermetallic plays a prominent role in the investigated mechanochemical process. Therefore, one can reasonably expect that the mechanochemical synthesis process begins with the reaction of Ti and W, with carbon leading to the formation of the respective most thermodynamically stable binary carbides (Figure 10b,c), followed by the diffusion between the TiC and WC grains, which produces the final (W,Ti)C solid solution. The binary carbides TiC and WC presumably formed not in a single step, but through a series of intermediate stable or metastable carbides, following the general sequences W–W₂C or W₉C₄–WC (Figure 10a) and Ti–Ti₂C–Ti₈C₅–TiC (Figure 10b). This proposed reaction sequence corresponds to the

previously reported mechanochemical synthesis of WC [51]. Likewise, the interaction between WC and TiC can produce intermediate ternary phase Ti_4WC_5 due to its relatively high formation energy (-0.662 eV/atom), until the formation of the single-phase solid solution (W,Ti)C is accomplished.

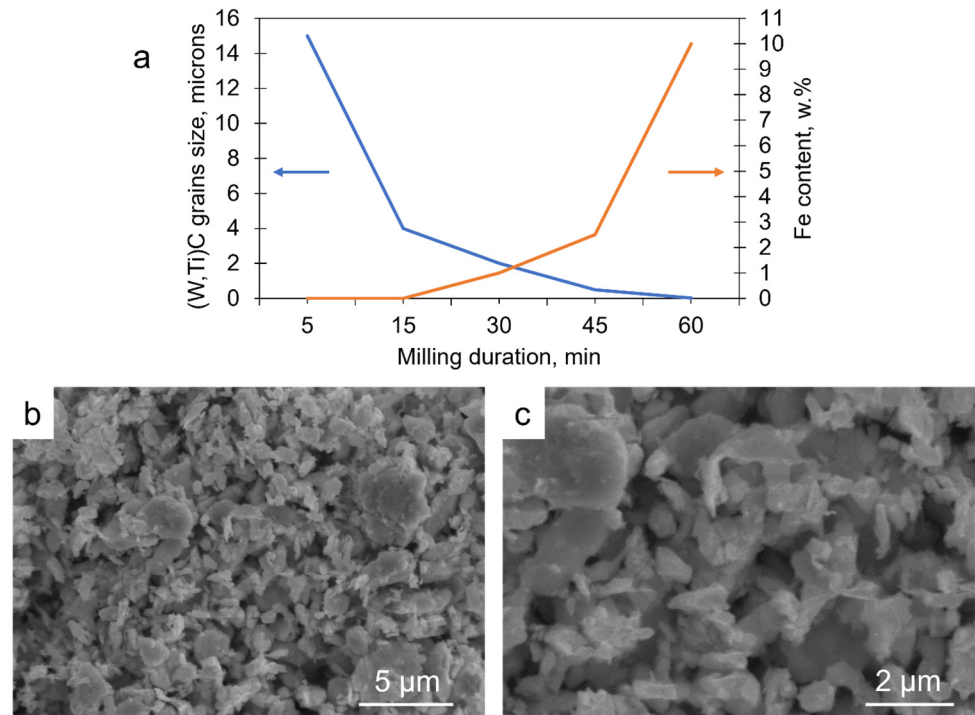


Figure 9. Dependence of grain size and Fe content on the duration of the mechanochemical synthesis (a); SEM micrographs of the (W,Ti)C powders after 15 min milling (b,c).

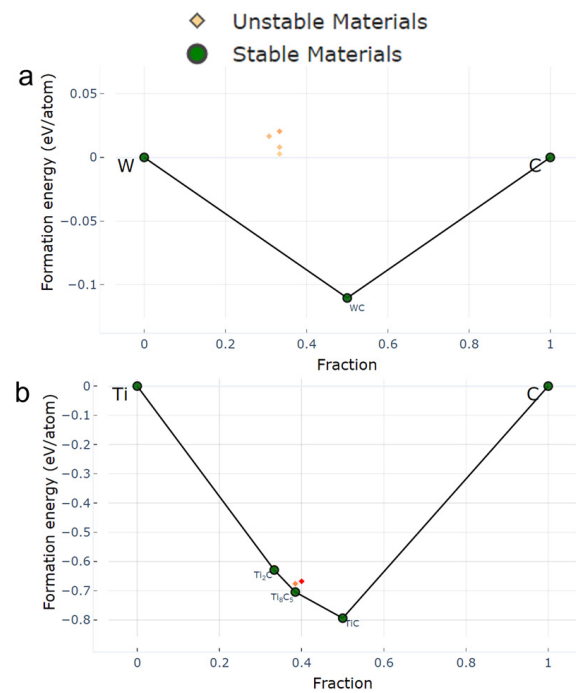


Figure 10. Interface reaction diagrams for systems W-C (a) and Ti-C (b).

3.6. Limitations and Further Scope for Improvement

The regression models developed in this work have some limitations, which should be addressed in the future. Although rare, instances of incorrect interpolation of data by the regression models do occur—as evident from some surprising local inflections in some of the main effect plots (left panels of Figures 4 and 6). One example is the curve corresponding to the effect of the ball-to-WC weight ratio during the ball milling of sintered WC on the WC grain size (Figure 6, left panel). This curve contains a minor inflection point around the ball-to-WC ratio of ~1.9, which has no physical meaning beneath it and is an artifact of the constructed regression equation. This problem can be mitigated by increasing the density of the dataset, thus reducing the interpolation errors. This approach is straightforward and fail-proof but inflates the number of necessary experiments. Another possible approach to remove the incorrect interpolations is to increase the number of members in the polynomial regression equation by introducing higher-degree parameter interactions. However, when a relatively low-density dataset is employed, introducing high-degree parameter interactions risks overfitting the model and decreasing its predictive power.

4. Conclusions

This work undertook a systematic parametric study on the three main stages of WC and TiC powder manufacturing—preparation of the green mixture, carbidization by furnace annealing, and ball milling of the annealed products. The influence of multiple parameters was investigated—carbon precursor, mass and diameter of milling bodies (balls), milling time and speed, temperature and duration of annealing, the height of powder in the furnace boats, and speed of movement of the furnace boats. Regression models for every stage of the process were verified by 10-fold validation and used to optimize the synthesis sequence, resulting in high-quality WC and TiC with a grain size below 2 microns and a content of free carbon below 0.1%. Additionally, solid solution (W,Ti)C was produced by mechanochemical synthesis from the elemental mixtures; however, the observed relatively high content of residual free carbon (0.2–0.8%) and contamination by Fe require further optimization of this process.

Supplementary Materials: The supplementary materials containing the initial datasets details of the statistical calculations can be downloaded at: <https://www.mdpi.com/article/10.3390/met12122144/s1>.

Author Contributions: Conceptualization, A.T., Z.E. and A.A.; Methodology, A.M., A.A., G.M. and M.A.; Software, M.A. and A.A.; Validation, M.A. and A.M.; Formal analysis, M.A. and G.M.; Investigation, M.A., A.M. and A.A.; Resources, R.S., Z.E. and D.M.; Data curation, A.A. and R.S.; Writing—original draft preparation, A.T. and A.A.; Writing—review and editing, A.T., A.A., D.M. and Z.E.; Supervision, Z.E. All authors have read and agreed to the published version of the manuscript.

Funding: The authors gratefully acknowledge financial support from project NTP No. O.003 Confidential "Creation of new composite materials with high performance properties based on rare and rare earth elements" on topic No. 5 "Development of fine-grained hard alloys of a new generation with high performance characteristics" of the Committee for Industrial Development of the Ministry industry and infrastructure development of the Republic of Kazakhstan.

Institutional Review Board Statement: Not applicable.

Informed Consent Statement: Not applicable.

Data Availability Statement: Not applicable.

Acknowledgments: The authors are grateful to Stepan Vorotilo for the thermodynamic calculations and statistical analysis of the experimental datasets.

Conflicts of Interest: The authors declare no conflict of interest.

References

1. García, J.; Collado Ciprés, V.; Blomqvist, A.; Kaplan, B. Cemented Carbide Microstructures: A Review. *Int. J. Refract. Met. Hard Mater.* **2019**, *80*, 40–68. [CrossRef]
2. Bobzin, K. High-Performance Coatings for Cutting Tools. *CIRP J. Manuf. Sci. Technol.* **2017**, *18*, 1–9. [CrossRef]
3. Bouzakis, K.-D.; Michailidis, N.; Skordaris, G.; Bouzakis, E.; Biermann, D.; M'Saoubi, R. Cutting with Coated Tools: Coating Technologies, Characterization Methods and Performance Optimization. *CIRP Ann.* **2012**, *61*, 703–723. [CrossRef]
4. Zhang, J.; Hassan Saeed, M.; Li, S. 13—Recent Progress in Development of High-Performance Tungsten Carbide-Based Composites: Synthesis, Characterization, and Potential Applications. In *Advances in Ceramic Matrix Composites*, 2nd ed.; Low, I.M., Ed.; Woodhead Publishing Series in Composites Science and Engineering; Woodhead Publishing: Cambridge, UK, 2018; pp. 307–329, ISBN 978-0-08-102166-8.
5. Jo, A.-R.; An, J.-S.; Kim, S.-H.; Jeong, M.-S.; Moon, Y.-H.; Hwang, S.-K. Novel Tensile Test Jig and Mechanical Properties of WC-Co Synthesized by SHIP and HIP Process. *Metals* **2021**, *11*, 884. [CrossRef]
6. Hoseinpour, A.; Vahdati Khaki, J.; Marashi, M.S. Mechanochemical Synthesis of Tungsten Carbide Nano Particles by Using WO₃/Zn/C Powder Mixture. *Mater. Res. Bull.* **2013**, *48*, 399–403. [CrossRef]
7. Radajewski, M.; Schimpf, C.; Krüger, L. Study of Processing Routes for WC-MgO Composites with Varying MgO Contents Consolidated by FAST/SPS. *J. Eur. Ceram. Soc.* **2017**, *37*, 2031–2037. [CrossRef]
8. Sun, J.; Zhao, J.; Gong, F.; Ni, X.; Li, Z. Development and Application of WC-Based Alloys Bonded with Alternative Binder Phase. *Crit. Rev. Solid State Mater. Sci.* **2019**, *44*, 211–238. [CrossRef]
9. Ojo-Kupoluyi, O.J.; Tahir, S.M.; Baharudin, B.T.H.T.; Azmah Hanim, M.A.; Anuar, M.S. Mechanical Properties of WC-Based Hardmetals Bonded with Iron Alloys—A Review. *Mater. Sci. Technol.* **2017**, *33*, 507–517. [CrossRef]
10. Panov, V.S. Nanostructured Sintered WC–Co Hard Metals (Review). *Powder Met. Met. Ceram.* **2015**, *53*, 643–654. [CrossRef]
11. Armstrong, R.W. The Hardness and Strength Properties of WC-Co Composites. *Materials* **2011**, *4*, 1287–1308. [CrossRef]
12. Bouleghlem, M.; Zahzouh, M.; Hamidouche, M.; Boukhobza, A.; Fellah, M. Microstructural and Mechanical Investigation of WC-TiC-Co Cemented Carbides Obtained by Conventional Powder Metallurgy. *Int. J. Eng. Res. Afr.* **2019**, *45*, 1–14. [CrossRef]
13. Kurlov, A.S.; Gusev, A.I.; Rempel, A.A. Vacuum Sintering of WC–8wt.% Co Hardmetals from WC Powders with Different Dispersity. *Int. J. Refract. Met. Hard Mater.* **2011**, *29*, 221–231. [CrossRef]
14. Zhang, Z.; Wahlberg, S.; Wang, M.; Muhammed, M. Processing of Nanostructured WC-Co Powder from Precursor Obtained by Co-Precipitation. *Nanostruct. Mater.* **1999**, *12*, 163–166. [CrossRef]
15. Kataria, R.; Kumar, J. Machining of WC–Co Composites—A Review. *Mater. Sci. Forum* **2015**, *808*, 51–64. [CrossRef]
16. Lin, H.; Sun, J.; Li, C.; He, H.; Qin, L.; Li, Q. A Facile Route to Synthesize WC–Co Nanocomposite Powders and Properties of Sintered Bulk. *J. Alloys Compd.* **2016**, *682*, 531–536. [CrossRef]
17. Correa, E.O.; Santos, J.N.; Klein, A.N. Microstructure and Mechanical Properties of WC Ni–Si Based Cemented Carbides Developed by Powder Metallurgy. *Int. J. Refract. Met. Hard Mater.* **2010**, *28*, 572–575. [CrossRef]
18. Huang, Z.; Ren, X.; Liu, M.; Xu, C.; Zhang, X.; Guo, S.; Chen, H. Effect of Cu on the Microstructures and Properties of WC-6Co Cemented Carbides Fabricated by SPS. *Int. J. Refract. Met. Hard Mater.* **2017**, *62*, 155–160. [CrossRef]
19. Genga, R.M.; Cornish, L.A.; Akdogan, G. Effect of Mo₂C Additions on the Properties of SPS Manufactured WC–TiC–Ni Cemented Carbides. *Int. J. Refract. Met. Hard Mater.* **2013**, *41*, 12–21. [CrossRef]
20. Mechanical-Property Relationships of Co/WC and Co-Ni-Fe/WC Hard Metal Alloys—ScienceDirect. Available online: <https://www.sciencedirect.com/science/article/pii/S026343689390049L?via%3Dihub> (accessed on 22 October 2022).
21. Chang, S.-H.; Chang, M.-H.; Huang, K.-T. Study on the Sintered Characteristics and Properties of Nanostructured WC–15 Wt% (Fe–Ni–Co) and WC–15 Wt% Co Hard Metal Alloys. *J. Alloys Compd.* **2015**, *649*, 89–95. [CrossRef]
22. Upadhyaya, G.S. Materials Science of Cemented Carbides—An Overview. *Mater. Des.* **2001**, *22*, 483–489. [CrossRef]
23. Dong, B.-X.; Qiu, F.; Li, Q.; Shu, S.-L.; Yang, H.-Y.; Jiang, Q.-C. The Synthesis, Structure, Morphology Characterizations and Evolution Mechanisms of Nanosized Titanium Carbides and Their Further Applications. *Nanomaterials* **2019**, *9*, 1152. [CrossRef] [PubMed]
24. Lee, K.H.; Cha, S.I.; Kim, B.K.; Hong, S.H. Effect of WC/TiC Grain Size Ratio on Microstructure and Mechanical Properties of WC–TiC–Co Cemented Carbides. *Int. J. Refract. Met. Hard Mater.* **2006**, *24*, 109–114. [CrossRef]
25. Brookes, K.J.A. *Hardmetals and Other Hard Materials*; International Carbide Data: London, UK, 1998; ISBN 978-0-9508995-6-5.
26. Lay, S.; Missiaen, J.-M. 1.03—Microstructure and Morphology of Hardmetals. In *Comprehensive Hard Materials*; Sarin, V.K., Ed.; Elsevier: Oxford, UK, 2014; pp. 91–120. ISBN 978-0-08-096528-4.
27. Andrén, H.-O. Microstructures of Cemented Carbides. *Mater. Des.* **2001**, *22*, 491–498. [CrossRef]
28. Weidow, J.; Zackrisson, J.; Jansson, B.; Andrén, H.-O. Characterisation of WC-Co with Cubic Carbide Additions. *Int. J. Refract. Met. Hard Mater.* **2009**, *27*, 244–248. [CrossRef]
29. Rolander, U.; Andrén, H.-O. Atom Probe Microanalysis of the γ Phase in Cemented Carbide Materials. *Mater. Sci. Eng. A* **1988**, *105–106*, 283–287. [CrossRef]
30. Chen, J.; Gong, M.F.; Wu, S.H. Flank Wear Mechanism of WC-5TiC-10Co Cemented Carbides Inserts When Machining HT250 Gray Cast Iron. *Appl. Mech. Mater.* **2014**, *670–671*, 517–521. [CrossRef]
31. Zhang, C.C.; Wang, Q.; Yuan, Q.Q.; Yang, Y.F.; Yi, X.L. Preparation of WC-5TiC-10Co Nanometer Powder and Performance Study of Sintering Samples. *Adv. Mater. Res.* **2012**, *465*, 220–223. [CrossRef]

32. Xiong, J.; Guo, Z.; Yang, M.; Wan, W.; Dong, G. Tool Life and Wear of WC–TiC–Co Ultrafine Cemented Carbide during Dry Cutting of AISI H13 Steel. *Ceram. Int.* **2013**, *39*, 337–346. [CrossRef]
33. Guo, Z.; Xiong, J.; Yang, M.; Dong, G.; Wan, W. Tool Wear Mechanism of WC–5TiC–10Co Ultrafine Cemented Carbide during AISI 1045 Carbon Steel Cutting Process. *Int. J. Refract. Met. Hard Mater.* **2012**, *35*, 262–269. [CrossRef]
34. Buravlev, I.Y.; Shichalin, O.O.; Papynov, E.K.; Golub, A.V.; Gridasova, E.A.; Buravleva, A.A.; Yagofarov, V.Y.; Dvornik, M.I.; Fedorets, A.N.; Reva, V.P.; et al. WC-5TiC-10Co Hard Metal Alloy Fabrication via Mechanochemical and SPS Techniques. *Int. J. Refract. Met. Hard Mater.* **2021**, *94*, 105385. [CrossRef]
35. Xing, J.; Foroughi, P.; Franco Hernandez, A.; Behrens, A.; Cheng, Z. Facile One-step High-temperature Spray Pyrolysis Route toward Metal Carbide Nanopowders. *J. Am. Ceram. Soc.* **2018**, *101*, 5323–5334. [CrossRef]
36. Manawi, Y.; Ihsanullah; Samara, A.; Al-Ansari, T.; Atieh, M. A Review of Carbon Nanomaterials' Synthesis via the Chemical Vapor Deposition (CVD) Method. *Materials* **2018**, *11*, 822. [CrossRef] [PubMed]
37. Moskovskikh, D.O.; Mukasyan, A.S.; Rogachev, A.S. Self-Propagating High-Temperature Synthesis of Silicon Carbide Nanopowders. *Dokl. Phys. Chem.* **2013**, *449*, 41–43. [CrossRef]
38. Mukasyan, A.S.; Shuck, C.E.; Pauls, J.M.; Manukyan, K.V.; Moskovskikh, D.O.; Rogachev, A.S. The Solid Flame Phenomenon: A Novel Perspective. *Adv. Eng. Mater.* **2018**, *20*, 1701065. [CrossRef]
39. Vidyuk, T.M.; Korchagin, M.A.; Dudina, D.V.; Bokhonov, B.B. Synthesis of Ceramic and Composite Materials Using a Combination of Self-Propagating High-Temperature Synthesis and Spark Plasma Sintering (Review). *Combust. Explos. Shock Waves* **2021**, *57*, 385–397. [CrossRef]
40. Rogachev, A.S. Mechanical Activation of Heterogeneous Exothermic Reactions in Powder Mixtures. *Russ. Chem. Rev.* **2019**, *88*, 875–900. [CrossRef]
41. Suryanarayana, C. Mechanical Alloying: A Novel Technique to Synthesize Advanced Materials. *Research* **2019**, *2019*, 4219812. [CrossRef]
42. Shkodich, N.; Sedegov, A.; Kuskov, K.; Busurin, S.; Scheck, Y.; Vadchenko, S.; Moskovskikh, D. Refractory High-Entropy HfTaTiNbZr-Based Alloys by Combined Use of Ball Milling and Spark Plasma Sintering: Effect of Milling Intensity. *Metals* **2020**, *10*, 1268. [CrossRef]
43. Mechanochemical Synthesis of Tungsten Carbide Powders Induced by Magnesiothermic Reduction of WCl₆ and Na₂CO₃ Raw Materials—IOPscience. Available online: <https://iopscience.iop.org/article/10.1088/2053-1591/ab2c34> (accessed on 2 December 2022).
44. Reva, V.P.; Onishchenko, D.V.; Petrov, V.V.; Kim, V.A.; Evstigneev, A.I. Formation of Hard Alloy VK8 Using Tungsten Carbide Powder Synthesized by Mechanochemical Technology. *Refract. Ind. Ceram.* **2013**, *54*, 295–298. [CrossRef]
45. Reva, V.P.; Onishchenko, D.V. Synthesis of Tungsten Carbide by Mechanically Stimulated Thermal Explosion of the WO₃-Mg-C System. *Combust. Explos. Shock Waves* **2014**, *50*, 68–74. [CrossRef]
46. Reva, V.P.; Onishchenko, D.V. Mechanochemical Synthesis of Tungsten Carbide with the Participation of Various Carbon Components. *Russ. J. Non-Ferr. Met.* **2014**, *55*, 57–64. [CrossRef]
47. Buinevich, V.S.; Nepapushev, A.A.; Moskovskikh, D.O.; Trusov, G.V.; Kuskov, K.V.; Mukasyan, A.S. Mechanochemical Synthesis and Spark Plasma Sintering of Hafnium Carbonitride Ceramics. *Adv. Powder Technol.* **2021**, *32*, 385–389. [CrossRef]
48. Nepapushev, A.A.; Kirakosyan, K.G.; Moskovskikh, D.O.; Kharatyan, S.L.; Rogachev, A.S.; Mukasyan, A.S. Influence of High-Energy Ball Milling on Reaction Kinetics in the Ni-Al System: An Electrothermographic Study. *Int. J. Self-Propag. High-Temp. Synth.* **2015**, *24*, 21–28. [CrossRef]
49. Reva, V.P.; Onishchenko, D.V.; Kuryavyi, V.G. Mechanochemical Synthesis Criteria for Titanium and Tungsten Carbides with Participation of Different Carbon Components. *Metallurgist* **2013**, *56*, 912–918. [CrossRef]
50. Reva, V.P.; Onishchenko, D.V. Tungsten Carbide Obtained by Mechanochemical Synthesis with the Use of Different Carbon Agents. *Met. Sci. Heat Treat.* **2013**, *55*, 275–280. [CrossRef]
51. Bolokang, S.; Banganayi, C.; Phasha, M. Effect of C and Milling Parameters on the Synthesis of WC Powders by Mechanical Alloying. *Int. J. Refract. Met. Hard Mater.* **2010**, *28*, 211–216. [CrossRef]
52. Koc, R.; Kodambaka, S.K. Tungsten Carbide (WC) Synthesis from Novel Precursors. *J. Eur. Ceram. Soc.* **2000**, *20*, 1859–1869. [CrossRef]
53. Wang, Q.; Wu, H.; Qin, M.; Li, Z.; Jia, B.; Chu, A.; Qu, X. Study on Influencing Factors and Mechanism of High-Quality Tungsten Carbide Nanopowders Synthesized via Carbothermal Reduction. *J. Alloys Compd.* **2021**, *867*, 158959. [CrossRef]
54. Ke, Z.; Zheng, Y.; Zhang, G.; Zhang, J.; Wu, H.; Xu, X.; Zhu, X. Microstructure and Mechanical Properties of WC-(Ti,W)C-Co Hardmetals Fabricated by in-Situ Carbothermal Reduction of Oxides and Subsequent Liquid Phase Sintering. *J. Alloys Compd.* **2021**, *865*, 158897. [CrossRef]
55. Ke, Z.; Zheng, Y.; Zhang, G.; Wu, H.; Xu, X.; Lu, X.; Zhu, X. Fabrication of Dual-Grain Structure WC-Co Cemented Carbide by in-Situ Carbothermal Reduction of WO₃ and Subsequent Liquid Sintering. *Ceram. Int.* **2020**, *46*, 12767–12772. [CrossRef]
56. Reddy, K.M.; Zou, X.; Hu, Y.; Zhang, H.; Rao, T.N.; Joardar, J. Influence of Heating Rate on Formation of Nanostructured Tungsten Carbides during Thermo-Chemical Processing. *Adv. Powder Technol.* **2021**, *32*, 121–130. [CrossRef]
57. Gao, L.; Kear, B.H. Synthesis of Nanophase WC Powder by a Displacement Reaction Process. *Nanostruct. Mater.* **1997**, *9*, 205–208. [CrossRef]

-
58. Schwetz, K.A.; Hassler, J. A Wet Chemical Method for the Determination of Free Carbon in Boron Carbide, Silicon Carbide and Mixtures Thereof. *J. Less Common Met.* **1986**, *117*, 7–15. [[CrossRef](#)]
 59. Bartel, C.J.; Millican, S.L.; Deml, A.M.; Rumpitz, J.R.; Tumas, W.; Weimer, A.W.; Lany, S.; Stevanović, V.; Musgrave, C.B.; Holder, A.M. Physical Descriptor for the Gibbs Energy of Inorganic Crystalline Solids and Temperature-Dependent Materials Chemistry. *Nat. Commun.* **2018**, *9*, 4168. [[CrossRef](#)] [[PubMed](#)]